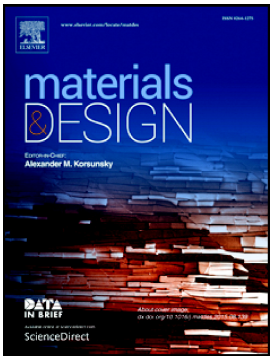

Influence of Ni in high Fe containing recyclable Al-Si cast alloys

C.B. Basak, Aditya Meduri, N. Hari Babu

PII: S0264-1275(19)30455-1
DOI: https://doi.org/10.1016/j.matdes.2019.108017
Article Number: 108017
Reference: JMADE 108017

To appear in: *Materials & Design*

Received date: 1 May 2019
Revised date: 2 July 2019
Accepted date: 4 July 2019

Please cite this article as: C.B. Basak, A. Meduri and N. Hari Babu, Influence of Ni in high Fe containing recyclable Al-Si cast alloys, Materials & Design, https://doi.org/10.1016/j.matdes.2019.108017

Influence of Ni in High Fe Containing Recyclable Al-Si Cast Alloys

C. B. Basak[*123], Aditya Meduri[3], N. Hari Babu[3]

[1] Mechanical Metallurgy Division, Bhabha Atomic Research Centre, Mumbai 400 085, India

[2] Homi Bhabha National Institute, Mumbai 400 094, India

[3] BCAST, Brunel University London, Uxbridge, UB8 3PH, UK

Abstract

Research in recycling Al-alloy is necessary for a sustainable industrial development. Iron present in the recycled Al-alloys deteriorates its mechanical properties. The challenge, therefore, is to tackle the iron impurity using different methodologies. The present study focuses on a strategy by which iron containing beta phase could be destabilized with the addition of Ni. A large number of microstructural image, lattice parameter data and mechanical properties have been obtained using optical microscopy with state-of-the-art image analysis, FESEM with EDS and EBSD, XRD, Vickers microhardness and universal tensile testing. Based on these results, the present work provide necessary insight about the effect of Ni addition in the recycled Al-Si cast alloys containing as high as 2wt% Fe. Finally it was concluded that upto 4wt% Ni addition could be beneficial for Al-Si alloys Si content limited to 9wt%.

1. Introduction

Energy requirement for the production of aluminium could be reduced by ten times by recycling the aluminium products rather than extracting the same from the bauxite ore[12] [1] [2]. However, the recycled aluminium accumulates different metallic impurities due to the diversified source of the scrap and also with the increasing number of recycling processes. Presence of these metallic impurities, either in solid solution or as a separate phase, poses a great challenge to obtain the same physico-mechanical properties as that of the virgin aluminium[34] [3, 4]. Therefore, the aim of the recycling could be shifted from making the commercially pure Al to developing a new castable Al-alloy with a different chemical composition. Such method of developing of new castable Al-alloy through recycling process enjoys a huge economical benefit[5] [5]. Despite the substantial energy saving and economic viability such newly developed alloy suffers from the accumulated metallic impurities, and amongst all metallic impurities Fe is known for its notoriety. In cast Al-alloys where Si is ubiquitous, Fe promotes the formation of the so-called β-

* Corresponding author: cbbasak@barc.gov.in

phase ($Al_9Fe_2Si_2$)[6,7] [6, 7]. It is now established that presence of Fe reduces the castability by reducing the fluidity of the melt and by increasing the porosity in the cast[8,9] [8, 9]. The network of β-phase, which appears as needle like feature in the micrograph, is directly responsible to reduce the strength and ductility of the alloy[10,11] [10, 11].

There exist different philosophies on how to tackle iron impurity in the recycled cast Al-alloy. Merits and disadvantages of each school of thoughts have been discussed elsewhere in details[5] [5]. It suffices here to briefly state the methodologies of tackling β-phase for the sake of the completeness; as mentioned below –

i) Removal of β-phase (and thereby iron impurity) by gravity segregation or by the filtration of the liquid metal[12] [12]

ii) Modification of the β-phase morphology by suitable heat treatment[7] [7]

iii) Destabilizing the β-phase by changing the chemical composition and promoting some other phase with or without further heat-treatment[6,13][6, 13]

The last method attracted many research works in the recent past; including the current one. For example, Mn was the first element identified as the modifier that promotes the formation of the polygonal $Al_{15}(Fe, Mn)_3Si_2$ phase rather than the β-phase, however, its effect vanishes beyond a Fe concentration of 1.2wt% in the Al-alloy[6] [6]. It was recently demonstrated that Cu can destabilized the β-phase by promoting the formation of ω-phase (Al_7Cu_2Fe)[13] [13]. The present work demonstrates Ni as the potential element to destabilize the β-phase and investigates its effect in the microstructure and the tensile properties of the modified Al-Si-Fe alloys with Si of 6wt%, 9wt% and 12wt% having a fixed Fe content of 2wt%.

2. Experimental

In these Al-Si-Fe-Ni alloys, three Si content were chosen, namely, 6wt%, 9wt% and 12wt% and for each Si content Ni was varied from 0wt% to 8wt% with an interval of 2wt% and Fe content was kept at a constant 2wt% for all these alloys. For the sake of brevity an alloy designated as 9Si6Ni would indicate an Al-alloy with a composition of 9wt% Si, 6wt% Ni, 2wt% Fe and the rest is Al. This style of designation will be used throughout in the rest of this article to refer a particular alloy composition.

99.95% pure Al ingots (from Norton Aluminium Ltd.), Al-50wt% Si, Al-45 wt% Fe and Al-20wt% Ni master alloys (from KBM Affilips) having commercial purity were used for preparing

the final alloys. Alloys of same Si content were prepared at a time in a pit type resistance furnace using boron nitride coated clay bonded graphite crucible. First Al ingot was melt and then Al-Si, Al-Fe and Al-Ni master alloys were added sequentially. A melt of about 400 g was prepared at 1306 K with intermittent stirring for a total holding time of 7200 s to ensure chemical homogeneity. Commercially available hexachloroethane (C_2Cl_6) tablet was used as degassing agent at 1023K before pouring into a boron nitride coated pre-heated (at 523 K) mild steel prismatic die with a cavity size of 150 mm x 70 mm x 20 mm. An average cooling rate of about 5-10 °C/s is expected based on previous experiments and experience[14][14]. Apart from the cast samples, homogenized specimens were made by cutting the cast samples pieces and isothermally holding at 823K for 48 hrs. followed by water quenching.

Standard metallographic technique with a final finish with 0.025µm colloidal silica polish was used for microstructural evaluation using both optical microscope and field emission scanning electron microscope (FESEM) fitted with energy dispersive spectroscope (EDS) and electron back scatter diffraction (EBSD) camera. Chemical composition of any particular phase, determined using EDS, reported here is based on the average value of 10 different measurements made in spot mode. Image analysis was carried out on the optical photomicrographs using ImageJ computer code[15] [15]. X-ray diffraction (XRD) traces were recorded using Bruker D8 machine that uses θ-θ goniometer with sample rotation; 1.6 kW Cu-K_α radiation with a step size of 0.01^o and 1 s dwell time at each step was used. Rietveld analysis of the XRD traces was carried out with GSAS II software[1617] [16, 17].Vickers microhardness testing were carried out as per ASTM E384-17 standard using 1 kg load and a dwell time of 10 s [18][18]. Rectangular shaped tensile samples were cut for tensile testing. Round and rectangular tensile specimens with some selected 9Si and 12Si alloy with varying Ni content upto 4wt% were made using high pressure die casting (HPDC). Sample dimensions and tensile test parameters conform to ASTM B557-10 standard[19] [19].

3. Results

Image analysis is a useful tool for determining the area fraction of multiple phases which might or might not appear in similar grey-scale level on lightly shaded matrix; thus the area fraction of matrix phase can also be determined. This data also corroborates the phase fraction (by volume) obtained from the XRD analysis. It is pertinent here to discuss about the technique deployed for

the image analysis in brief. Many a times the optical micrograph suffers from partial shadowing due to slightest obliqueness on the polished surface and image analysis of such unprocessed raw images becomes difficult, sometimes impossible. One of the best ways to tackle the partial shadowing issue is usage of FFT (Fast Fourier Transformation) assisted band pass filter, followed by contrast enhancement and color thresholding. Optical photomicrographs along with different snapshots of the image analysis stages of the as-cast samples are provided in the fig. 1, 2 and 3 for different Si content respectively. Similar figures for the samples homogenized at 550^{o}C for 48 hrs. are presented in the supplementary fig. S1, S2 and S3. Area fraction of the matrix phase calculated from the image analysis for all the samples are presented in the Table 1 and compared with that of homogenized samples in supplementary table S1.

Lattice parameters and the phase fractions obtained from the Rietveld analysis along with the matrix area fractions calculated from the image analysis are presented in Table 1. Whole pattern fitting of the XRD traces for Rietveld analysis for the as-cast samples could be found in the supplementary fig. S4 (a- l). It is worthwhile to note that area fraction and volume fraction would never match even for the uniformly distributed equal sized spherical particle as a second phase; nonetheless, area fraction and volume fraction has a one to one correspondence between them[20] [20].

To see the efficacy of the present thermodynamic database for Al-alloys and to compare the thermodynamic results with the XRD data MatCalc (v.6.03) computer code with Al-alloy database from Hao et. al. was used[21] [21]. Both Scheil solidification and equilibrium solidification model was adopted and corresponding yield of the intermetallic phases were present in fig. 4 (a-d). Isopleths were constructed at 6wt%, 9wt% and 12wt% Si content with fixed 2wt%Fe; as presented in supplementary fig. S5, using both MatCalc and PandaT softwares without and with Hao's database, respectively.

SEM micrograph of as-cast 6Si2Ni sample is presented in fig. 5 (a) and corresponding elemental mapping of Si-K_{α}, Fe-K_{α} and Ni-K_{α}.using EDS are presented in fig. 5 (b- d) respectively. SEM micrograph of as-cast 12Si2Ni sample is presented in fig. 6 (a) and corresponding elemental mapping of Si-K_{α}, Fe-K_{α} and Ni-K_{α}.using EDS are presented in fig. 6 (b- d) respectively. Fig. 7 (a-b) and (c-d) are the bright field optical photomicrographs showing the effect of homogenization on the morphological changes of the phases in the 12Si2Ni and 12Si4Ni alloys, respectively. An SEM image of 9Si2Ni sample homogenized at 550^{o}C for 48hrs

showing the growth of Al_9FeNi phase on the edge of β-$Al_9Fe_2Si_2$ phase is presented in fig. 8 (a) and corresponding quantitative line scan is shown in fig. 8 (b). Growth of Al_9FeNi phase along the edge of the β-$Al_9Fe_2Si_2$, similar to fig. 8 (a), can be seen at lower magnification in the supplementary fig. S6. The elemental mapping of 12Si4Ni sample homogenized at 550^{o}C for 48 hrs suggesting the growth of Al_9FeNi phase onto the β-$Al_9Fe_2Si_2$ phase could be seen in supplementary fig. S7 (a-d). Screen shots of Kikuchi pattern analysis from the electron back scattered pattern (EBSP) of homogenized 12Si4Ni sample can be seen in supplementary fig. S8 (a-b). Fig 10 (a) and (b) is the SEM image and the corresponding band contrast image (difference between maximum intensity of a Kikuchi band in the electron back scattered pattern (EBSP) and the background intensity in the pattern) of homogenized 9Si8Ni sample; whereas fig. 9 (c) and (d) is the phase map and Euler map, respectively, of the same area considering Al_9FeNi and Al_3Ni phase. Fig. 9 (e- h) represents the elemental mapping of the same area using Al K_α, Si K_α, Ni K_α and Fe K_α x-ray respectively.

Fig. 10 shows variation in Vickers microhardness with respect to the Ni content in the alloy for both as-cast and homogenized condition. Yield stress at 0.2% offset strain, ultimate tensile strength (UTS) and elongation till failure are plotted in fig. 11 (a- c), respectively, with the varying Ni content in the alloy. The original engineering stress vs. strain curves for the as-cast alloys can be found in the supplementary fig. S9 and the same for the HPDC samples are presented fig. S10.

4. Discussions

4.1 Microstructure

It has been shown earlier that, for a given concentration of Fe, the formation of β-phase ($Al_9Fe_2Si_2$) requires a minimum level of Si concentration in Al-Fe-Si system[7] [7]. In the present alloys Fe was kept constant at 2wt%, as a minimum Si content of 1.5wt% is required for the formation of β-$Al_9Fe_2Si_2$ phase[7] [7]. However, juxtaposing fig.1 and table 1 it can be seen that microstructure of 6Si alloys does not contain the characteristic needle like β-$Al_9Fe_2Si_2$ phase. On the other hand, comparing fig. 3 and table 1 it can be seen that in case of 12Si alloys the phase fraction of β-$Al_9Fe_2Si_2$ dwindles as Ni content increases in the alloy. Therefore it can be said with certainty that addition of Ni tends to destabilize the β-$Al_9Fe_2Si_2$ and favors the formation of Al_9FeNi phase; also, this destabilization effect is strong at low Si content. Table 1 also ascertains

that formation of Al_3Ni phase requires a minimum amount of Ni addition for a given amount of Fe content. Hao et. al. has also shown earlier that in Al-8wt%Si-1wt%Fe alloy addition of even 1wt% Ni destabilized β-$Al_9Fe_2Si_2$ phase formation[21] [21].

It is important to note that β-phase forms in needle like morphology, as shown in 12Si samples (fig. 3 top two rows); whereas Al_9FeNi phase forms in polygonal morphology as shown in fig. 5 (a- d). Coexistence of Fe and Ni, as shown in fig. 5 (c- d), by EDS assisted elemental mapping and XRD analysis proves complete annihilation of β-$Al_9Fe_2Si_2$ phase and presence of Al_9FeNi phase in as-cast 6Si2Ni. On the other hand, SEM micrographs and elemental maps of as-cast 12Si2Ni sample show the coexistence of both β-$Al_9Fe_2Si_2$ phase and presence of Al_9FeNi phase, as evident from the fig. 6 (a- d) and supported by the XRD analysis (table 1).

Effect of homogenization on the Si and β-phase are well known and the probable mechanisms of morphological changes are also proposed for the Al-Fe-Si system[7] [7]. Addition of Ni does not play any significant role in changing the morphology of Si. The morphological changes of phases in 12Si2Ni and 12Si4Ni sample is rather apparent as presented in the fig. 7 (a- b) and (c- d), respectively; where the blocky Si particles in as-cast microstructure tend to be spherodized, the β-$Al_9Fe_2Si_2$ phase and Al_9FeNi phase gets fragmented in sausage like morphology. The compositional changes of different phases will be discussed in the next section.

In case of higher Ni content alloys the Al_3Ni phase usually forms onto the matrix- Al_9FeNi interface as presented in the fig. 9 (a- c). The phase map image generated by indexing Kikuchi patterns, in fig. 9 (c), is particularly important to identify the Al_9FeNi phase (blue colored) and Al_3Ni phase (red colored) distinctly. It was observed during Rietveld fitting that both Al_9FeNi phase and Al_3Ni phase required higher order of spherical harmonics (often more than 6^{th} order), signifying highly textured phase. The same could be reconfirmed through orientation mapping (Euler angle) as presented in fig. 9 (d); it shows identical coloring for Al_9FeNi phase disjoint across the spatial scale indicating that this phase posses high degree of crystallographic preferred orientation. Similar comment can also be made for the Al_3Ni phase, in fact texture index for this phase is even higher than the Al_9FeNi phase, as revealed during Rietveld analysis. It needs to mention here that Al and Si phase was not considered during the indexing of Kikuchi pattern since the phase map and orientation map would look extremely cluttered and the very purpose of showing Al_9FeNi and Al_3Ni phase would go in vein. Fig. 9 (e-h) is the elemental mapping corroborating the presence of these phases. It is important to note here that even after

homogenization treatment no major change was observed in terms of the phase fraction, except for the fact the more Al_9FeNi phase forms with the expense of β-$Al_9Fe_2Si_2$ phase. The homogenization treatment does not alter the crystallographic orientation of Al_9FeNi and Al_3Ni phase as well, as could be observed from the fig. 9 (d).

4.2 Phase composition

It is known that β-$Al_9Fe_2Si_2$ phase is highly faulted structure and because of that it has considerable capacity in accommodating other elements (e.g. Cu etc.) into its lattice by suitable site substitution[22] [22]. In 12Si2Ni alloy, EDS analysis reveals that Ni can replace the Fe atoms in the β-$Al_9Fe_2Si_2$ phase; in as-cast condition about 13% of Fe sites were occupied by the Ni atom and upon homogenization Ni occupies about half of the Fe sites in the β-$Al_9Fe_2Si_2$ phase; however, no alteration in Si content was observed in these two cases. Therefore, under equilibrium condition the β-$Al_9Fe_2Si_2$ phase in 6Si2Ni alloy can be expressed as $Al_9(Fe_{0.5}Ni_{0.5})_2Si_2$. Similar site occupancy of β-$Al_9Fe_2Si_2$ phase gives better fitting during the Rietveld analysis of XRD data.

EDS analysis shows that in as-cast 6Si2Ni sample the Al_9FeNi phase contains 2at%Si, more than 13at% Fe and about 8at% Ni against the theoretical value of about 9.1 at% for Fe and Ni. Upon homogenization it was observed that while Fe decreases slightly to reach 11at%, the Si content increases in Al_9FeNi phase from 2at% to upto 6.5 at%; and Ni too approaches 6.5at% from 8at%. However, it was observed that the sum of Si content and Ni content remains nearly equal to Fe content. It needs to be emphasized here that in Al_9FeNi phase both Fe and Ni occupy the same site since Al_9FeNi phase is crystallographically equivalent to Al_9Co_2 prototype[23] [23]. Therefore, in case of 6Si2Ni alloy the equilibrium Al_9FeNi phase can actually be expressed as $Al_9Fe_x(Si_{0.5},Ni_{0.5})_{2-x}$, where x is slightly less than 1 and solely depends on the alloy composition. Similarly, in case of homogenized 12Si8Ni alloy Al_9FeNi phase can be approximated as $Al_9(Fe_{0.67}Si_{0.33})Ni$, since Fe was about 6at% and approximately twice than that of Si content, however, sum of Si and Fe content remains nearly equal to the Ni content. Therefore, it could be said that in the low-Si low-Ni end in 2wt% Fe isopleths of Al-Fe-Si-Ni system (e.g. 6Si2Ni) Fe:Si:Ni is equals to 2:1:1 in Al_9FeNi phase; whereas in high-Si high-Ni end (e.g. 12Si4Ni and 12Si8Ni) the ratio was found to be 2:1:3 as sum of Fe and Si content equals to the Ni content. Interestingly, in 12Si2Ni sample the chemical composition of Al_9FeNi phase reveals the ratio of Fe:Si:Ni as 1:1:1.

It is rather clear from the EDS line scanning that during homogenization part of β-$Al_9Fe_2Si_2$ phase gets converted to Al_9FeNi phase at the β-matrix interface, as evident from the fig. 8 (a-b). This observation highlights the fact that Ni tends to destabilize β-$Al_9Fe_2Si_2$ phase and promotes the formation of the Al_9FeNi phase. Despite the usual limitation of the EDS technique in terms of the certainty in the chemical composition, the relative changes of Si, Fe and Ni in Al_9FeNi phase clearly indicates large solubility range of these elements in that intermetallic phase; however, effect of chemical composition is not very apparent in their lattice parameters when as-cast samples are considered.

4.3 Phase diagram and solidification

At this point it is imperative to compare the phase fractions obtained from the XRD data with the same obtained from the thermodynamic calculations. Therefore, to obtain the yield of different intermetallic phases both Scheil solidification model and equilibrium solidification model were considered. It is known that for the substitutional alloys Scheil solidification model works with reasonable accuracy [24][24]. MatCalc software was used alongwith Hao's database for assessing the solidification and yield of the intermetallic phases [21][21]. Fig. 4 (a), (b) and (c) represent yield (in wt%) of β-$Al_9Fe_2Si_2$, Al_9FeNi and Al_3Ni phase as obtained from the Scheil solidification calculation. Fig. 4 (a) clearly shows the efficacy of Ni in destabilizing the $Al_9F_2Si_2$ phase in low-Si alloys; e.g. in 6Si alloy only 2wt%Ni is enough to destabilize β-$Al_9F_2Si_2$ phase, whereas in 12Si alloy the same could be achieved with 4wt%Ni. On the other hand fig. 4 (b) and (c) depicts increasing yield of Al_9FeNi and Al_3Ni phases, respectively, with increase in Ni content in an alloy for a given Si content. This trend is similar to that observed from the XRD results as well (see Table 1). Fig. 4 (d) represents the yield of Al_9FeNi, the only intermetallic phase obtained as per the equilibrium solidification. It is interesting to note that the phase fraction and the trend pertaining to the yield of Al_9FeNi phase obtained from the XRD analysis match fairly well to the same obtained from the equilibrium solidification calculation (fig. 4-d).

Supplementary fig. S5 represents the isopleths calculated by MatCalc with their Al-database (top row) and the same using PandaT software with Hao's database[21][21]. Isopleths obtained from MatCalc databse does not show the Al_9FeNi as the stable phase at the room temperature; whereas Hao's database does not show Al_3Ni as the stable phase. It is clear from the fig. S5 that these isopleths differ considerably in terms of temperature, phase stability and the phase boundary.

In Al_9FeNi crystal structure, the Fe and Ni sites are equivalent and therefore it was seen that Si can replace both Fe and Ni depending on the Si and Ni content of the alloy; therefore Al_9FeNi phase can take up a large amount of Si; as discussed in detail in the previous section with the help of EDS result. On the other hand, as discussed earlier, Ni can replace as high as half of the Fe sites in $Al_9Fe_2Si_2$ phase at higher temperature and rejects Ni at lower temperature. Therefore, it seems reasonable to assume that both Si and Ni play a significant role in deciding the relative stability of the Al_9FeNi and $Al_9Fe_2Si_2$ phase, respectively.

4.4 Mechanical properties

The micro-hardness value of the both as-cast and homogenized alloys monotonously increases with increasing Ni, as shown in fig. 10 (a-b). The overall increase in hardness with increasing Si and Ni is due to the higher yield of the intermetallic phases, e.g. Al_9FeNi and Al_3Ni. However, homogenization treatment decreases the hardness and the extent of decrease is more at higher Si and Ni content. Such decrease is expected due to several reasons, e.g. chemical equilibration between matrix phase and intermetallic phases; the spheroidization of different phases that eliminates the stress concentration to a larger extent, as evident in fig. 7 (b) and (d).

The 0.2% yield stress and UTS are found higher in high pressure die cast (HPDC) sample than corresponding gravity mold cast sample, as can be seen from fig. 11 (a-b); however, the ductility of HPDC sample deteriorates beyond about 4wt%Ni. Overall it is apparent that irrespective of the Si content and the casting technique the alloy composition beyond 4wt%Ni reduces the ductility. It can be assumed safely that the ductility is not dependent on the size of the dendrites as the ductility does not vary much from gravity cast (GC) to HPDC samples for a given composition, see fig. 11 (c), despite huge difference in the cooling rate that determines the inter-dendritic spacing. Therefore, in the present case the ductility is chiefly a function of the fraction of the intermetallic phase. On the other hand due to higher cooling rate in HPDC the nucleation rate was also higher and therefore the intermetallic phases were finely distributed over the casting this result into the significant rise in the yield strength and UTS.

5. Conclusions

i. β-$Al_9Fe_2Si_2$ phase exhibits solubility for Ni, where Ni occupies Fe sites.

ii. Al_9FeNi phase shows appreciable solubility for Si and Si can replace both Fe and Ni depending on the Si and Ni content of the alloy.

iii. Present thermodynamic description is indecisive about the stability of Al_9FeNi and Al_3Ni phase below 550^oC.

iv. Ni destabilizes β-$Al_9Fe_2Si_2$ phase and favors formation of Al_9FeNi phase in Al-Si-Fe-Ni alloy system; the effect of destabilization is strong in high Fe containing Al-alloys with Si content less than 9wt%.

v. Ni addition is beneficial in high-Fe Al-Si cast alloy with low-Si content of below 9wt%; however, Ni content of more than 4wt% deteriorates the mechanical properties of the alloys.

Acknowledgements

The present work has been carried out under the aegis of Marie Sklodowska Curie Individual Fellowship (MSCA-IF-2014) awarded by European Commission (EU project no. 656943). Author CBB greatly acknowledges the help from Prof. Ernst Kozeschnik, Vienna University of Technology, Austria for providing the trial license of MatCalc (v. 6.03) and Dr. Chuan Zhang, CompuTherm LLC, US for providing the isopleths generated with PandaT software.

Data availability

Some of the raw data required to reproduce these findings are available to download from the DOI [DOI- 10.17633/rd.brunel.8047325].

Table 1: Matrix area (%) obtained from the image analysis; while the phase fractions (wt%) and the lattice parameters were obtained from the Reitveld analysis of the XRD traces.

Phase details	**As-cast samples**														
	6Si0Ni	**6Si2Ni**	**6Si4Ni**	**6Si6Ni**	**6Si8Ni**	**9Si0Ni**	**9Si2Ni**	**9Si4Ni**	**9Si6Ni**	**9Si8Ni**	**12Si0Ni**	**12Si2Ni**	**12Si4Ni**	**12Si6Ni**	**12Si8Ni**
Matrix area (%)	79.95	78.69	73.95	64.13	59.5	76.04	72.62	65.95	62.4	62.06	73.03	67.13	58.73	55.8	48.15
Al (wt%)	**88.70**	**79.10**	**71.80**	**55.80**	**57.70**	**84.50**	**82.10**	**65.80**	**54.40**	**57.20**	**81.60**	**77.00**	**74.80**	**56.20**	**53.50**
a (nm)	0.404949	0.404945	0.404782	0.404860	0.404973	0.404923	0.404769	0.404795	0.404751	0.404836	0.404944	0.404793	0.405062	0.404922	0.405077
Si (wt%)	**5.60**	**4.40**	**5.80**	**6.10**	**5.90**	**8.70**	**8.80**	**8.70**	**8.90**	**8.40**	**11.20**	**11.10**	**11.80**	**12.00**	**11.70**
a (nm)	0.542925	0.542920	0.542884	0.543038	0.542947	0.542888	0.542926	0.542908	0.542857	0.542975	0.542966	0.542993	0.543074	0.543053	0.543070
$Al_9Fe_2Si_2$ (wt%)	**5.70**	**0.00**	**0.00**	**0.00**	**0.00**	**6.80**	**0.50**	**0.00**	**0.00**	**0.00**	**7.20**	**5.70**	**0.40**	**0.00**	**0.00**
a (nm)	2.080913	--	--	--	--	2.081133	2.081336	--	--	--	2.075920	2.080813	2.065831	--	--
b (nm)	0.617934	--	--	--	--	0.618321	0.618275	--	--	--	0.618855	0.618053	0.613595	--	--
c (nm)	0.616423	--	--	--	--	0.621666	0.616360	--	--	--	0.622213	0.616324	0.636641	--	--
β (degree)	91.343	--	--	--	--	91.223	90.394	--	--	--	91.261	90.544	92.597	--	--
Al_9FeNi (wt%)	**--**	**16.50**	**22.40**	**34.00**	**32.30**	**--**	**8.60**	**25.50**	**31.90**	**27.10**	**--**	**6.20**	**13.00**	**27.30**	**27.30**
a (nm)	--	0.621630	0.622572	0.623329	0.622692	--	0.622773	0.622753	0.622325	0.622926	--	0.619604	0.622310	0.622587	0.622191
b (nm)	--	0.627480	0.627798	0.628656	0.627722	--	0.627061	0.627226	0.627423	0.627361	--	0.627209	0.626257	0.626855	0.625800
c (nm)	--	0.859648	0.858079	0.859615	0.859591	--	0.858330	0.858940	0.859061	0.860001	--	0.861804	0.859298	0.859553	0.859476
β (degree)	--	94.799	94.919	95.247	95.219	--	94.936	95.045	95.093	95.210	--	95.335	95.253	95.243	95.203
Al_3Ni (wt%)	**--**	**0.00**	**0.00**	**4.10**	**4.10**	**--**	**0.00**	**0.00**	**4.80**	**7.30**	**--**	**0.00**	**0.00**	**4.50**	**7.50**
a (nm)	--	--	--	0.660420	0.660069	--	--	--	0.660665	0.660929	--	--	--	0.661013	0.660845
b (nm)	--	--	--	0.734301	0.733983	--	--	--	0.736906	0.736247	--	--	--	0.733793	0.734001
c (nm)	--	--	--	0.481897	0.481916	--	--	--	0.481041	0.481294	--	--	--	0.481087	0.481047
R_{wp} (%)	7.11	10.59	10.05	7.87	8.54	8.31	11.46	10.90	10.93	9.61	7.32	9.57	9.4	8.54	8.24

Fig. 1. From top row to bottom row, 6Si0Ni, 6Si2Ni, 6Si4Ni, 6Si6Ni and 6Si8Ni as-cast samples. As-obtained micrographs are in the first column; second column is FFT filtered and contrast adjusted and the last one is thresholded micrographs for calculating area fraction.

Fig. 2. From top row to bottom row, 9Si0Ni, 9Si2Ni, 9Si4Ni, 9Si6Ni and 9Si8Ni as-cast samples. As-obtained micrographs are in the first column; second column is FFT filtered and contrast adjusted and the last one is thresholded micrographs for calculating area fraction.

Fig. 3. From top row to bottom row, 12Si0Ni, 12Si2Ni, 12Si4Ni, 12Si6Ni and 12Si8Ni as-cast samples. As-obtained micrographs are in the first column; second column is FFT filtered and contrast adjusted and the last one is thresholded micrographs for calculating area fraction.

Fig. 4. Yield of different intermetallic phases at the end of solidification (a) β-$Al_9Fe_2Si_2$, (b) Al_9FeNi and (c) Al_3Ni; using Scheil solidification model. Only intermetallic phase, i.e. Al_9FeNi, was found stable under equilibrium solidification model and the corresponding yield is presented in (d).

Fig. 5. As-cast 6Si2Ni sample showing (a) SEM micrograph and corresponding elemental mapping of (b) Si-K_α, (c) Fe-K_α and (d) Ni-K_α. The coexistence of Fe and Ni in the composition of the dispersed phase and corresponding Kikuchi pattern (not shown here) confirms Al_9FeNi phase.

Fig. 6. SEM micrograph and elemental mapping of as-cast 12Si2Ni sample; (a) SEM micrograph, (b) Si Kα, (c) Fe Kα and (d) Ni Kα. The composition of the needle-like phase reveals β-$Al_9Fe_2Si_2$ (dotted arrow) coexisting with Al_9FeNi phase (solid arrow).

Fig. 7. Bright field optical photomicrograph of 12Si2Ni and 12Si4Ni sample in as-cast condition (a) and (c) respectively; and after homogenization (b) and (d). The darkest shaded phase is Si and the rest are either β-phase or Al_9FeNi phase in the Al-matrix. Note the change in phase morphology after homogenization.

Fig. 8. (a) SEM micrograph showing β-phase needle with growing Al_9FeNi phase along its edge in 9Si2Ni sample homogenized at 550^{o}C for 48hrs, the dashed line indicates line scan direction and (b) EDS line scan for quantitative elemental analysis across the β-phase needle.

Fig. 9. EBSD assisted phase map and simultaneous EDS elemental mapping 9Si8Ni sample homogenized at 550^{o}C for 48hrs for the phase identification; (a) SEM image, (b) band contrast image, (c) phase map showing coexisting Al_9FeNi phase (blue) and Al_3Ni phase (red), note that Al and Si were not considered during the indexing of Kikuchi pattern, (d) Orientation map showing Al_9FeNi phase and Al_3Ni phase excluding Al and Si phase. EDS assisted elemental mapping showing (e) Al-K_α, (f) Si-K_α, (g) Ni-K_α and (h) Fe-K_α.

Fig. 10. Vickers microhardness of gravity cast alloys as a function of Ni content in as-cast condition and after homogenization at 550^{o}C for 48hrs.

Fig. 11. Tensile properties of as-cast sample, (a) yield strength, (b) UTS and (c) elongation at failure, GC stands for gravity casting and HPDC for high pressure die casting

References

[1] J. A. S Green (ed), Aluminum recycling and processing for energy conservation and sustainability, ASM International, USA (2007) 15

[2] C. Schmitz (ed), Handbook of aluminium recycling, Vulkan Verlag, Germany (2006) 25

[3] S. K. Das, J. A. S. Green, J. G. Kaufman, D. Emadi, M. Mahfoud, Aluminium recycling – An integrated industrial approach, JOM 62 (2) (2010) 23

[4] A.Gesing, Assuring the continued recycling of light metals in end-of-life vehicles: A global perspective, JOM 56 (8) (2004)18

[5] C. B. Basak, N. Haribabu, Improved Recyclability of cast Al-alloys by engineering β-$Al_9Fe_2Si_2$phase, Light Metals 2017, ed. A. P. Ratvik, Spinger International Publishing (2017) 1139

[6] S.G. Shabestari,The effect of iron and manganese on the formation of intermetallic compounds in aluminum–silicon alloys, Mat. Sci. Eng. A 383 (2004) 289

[7] C. B. Basak, N. Haribabu, Morphological changes and segregation of β-$Al_9Fe_2Si_2$ phase: A perspective from better recyclability of cast Al-Si alloys, Mater. Des. 108 (2016) 277

[8] E. Taghaddos, M.M. Hejazi, R. Taghiabadi, S.G. Shabestari, Effect of iron-intermetallics on the fluidity of 413 aluminum alloy, J. Alloy. Comp. 468 (2009) 539

[9] Z. Ma, A.M. Samuel, F.H. Samuel, H.W. Doty, S. Valtierra,A study of tensile properties in Al–Si–Cu and Al–Si–Mg alloys: Effect of β-iron intermetallics and porosity, Mater Sci Eng A, 490 (2008) 36

[10] J.Z. Yi, Y.X. Gao, P. D. Lee, T.C. Lindley,Effect of Fe-content on fatigue crack initiation and propagation in a cast aluminum–silicon alloy (A356–T6), Mater. Sci. Eng. A 386 (2004) 396

[11] S. Ji, W. Yang, F. Gao, D. Watson, Z. Fan, Effect of iron on the microstructure and mechanical property of Al–Mg–Si–Mn and Al–Mg–Si diecast alloys, Mater. Sci. Eng. A 564 (2013) 130

[12] H. L. de Moraes, J. R. de Oliveira, D. C. R. Espinosa, J. A. S. Tenorio, Removal of iron from molten recycled aluminum through intermediate phase filtration, Mater. Tran. 47(7) (2006) 1731

[13] C. B. Basak, N. Haribabu, Influence of copper in modifying the beta phase and enhancing the mechanical properties of recycled Al-Si-Fe cast alloys, Sci. Rep. 7 (2017) 5779

[14] A. Gorny, J. Manickaraj, Z. Cai, S Shankar, Evolution of Fe based intermetallic phases in Al–Si hypoeutectic casting alloys: Influence of the Si and Fe concentrations, and solidification rate, J. Alloy Com. 577 (2013) 103

[15] C. A. Schneider, W. S. Rasband, K. W. Eliceiri, NIH Image to ImageJ: 25 years of image analysis, Nat. Methods, 9 (2012) 671

[16] A.C. Larson, R.B. Von Dreele, General Structure Analysis System (GSAS), Los Alamos National Laboratory Report LAUR 86-748 (2000)

[17] B. H. Toby, EXPGUI: a graphical user interface for GSAS, J. Appl. Cryst. 34 (2001) 210

[18] ASTM E384-17, Standard test method for microindentation hardness of materials, ASTM International, West Conshohocken, PA, (2017) www.astm.org

[19] ASTM B557-10, Standard Test Methods for Tension Testing wrought and cast aluminium and magnesium alloy product, ASTM International, West Conshohocken, PA, (2015) www.astm.org

[20] C. B. Basak, A. K. Sengupta,Development of a FDM based code to determine the 3-D size distribution of homogeneously dispersed spherical second phase from microstructure: a case study on nodular cast iron, Scripta. Mater. 51 (2004) 255

[21] D. Hao, B. Hu, K. Zhang, L. Zhang, Y. Du The quaternary Al–Fe–Ni–Si phase equilibria in Al-rich corner: experimental measurement and thermodynamic modeling, J. Mater. Sci. 49 (2014) 1157

[22] V. Hansen, B. C. Hauback, M. Sundberg, J. Gjonnes, β-$Al_{4.5}$FeSi: A combined synchrotron powder diffraction, electron diffraction, high-resolution electron microscopy and single-crystal x-ray diffraction study of a faulted structure, Acta. Cryst. B 54 (1998) 351

[23] I. Chumak, K. W. Richter, H. Ipser, The Fe-Ni-Al phase diagram in the Al-rich (>50 at.% Al) corner, Intermetallics 15 (2007) 1416

[24] C. B. Basak, M. Krishnan, Applicability of Scheil-Gulliver solidification model in real alloy: study with Cu-9wt%Ni-6wt%Sn, Phil. Mag. Let. 95 (7) (2015) 376

Credit Author Statement

Author#1: Experimental design, experiments, analysis, manuscript writing

Author#2: Experiments, analysis

Author#3: Experiments, manuscript writing, Internal review

Highlights

- β-$Al_9Fe_2Si_2$ phase exhibits solubility for Ni, where Ni occupies Fe sites.
- Si can replace both Fe and Ni sites in Al_9FeNi phase.
- Ni destabilizes β-$Al_9Fe_2Si_2$ phase and promotes Al_9FeNi phase.
- Destabilization of β-$Al_9Fe_2Si_2$ phase due to Ni is more prominent when Si content is less than 9wt%.
- Ni content of more than 4wt% deteriorates the mechanical properties of the alloys.

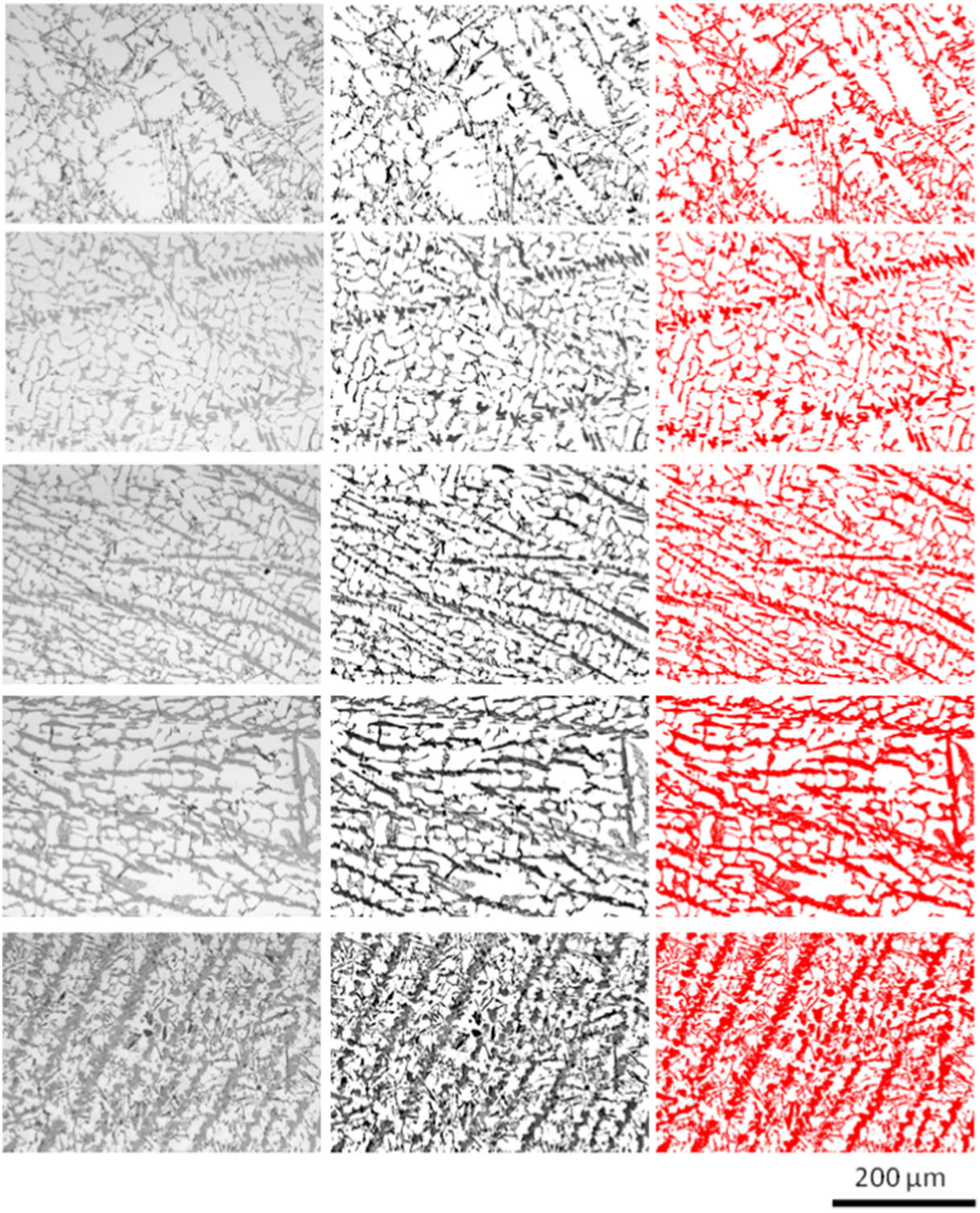

Figure 1

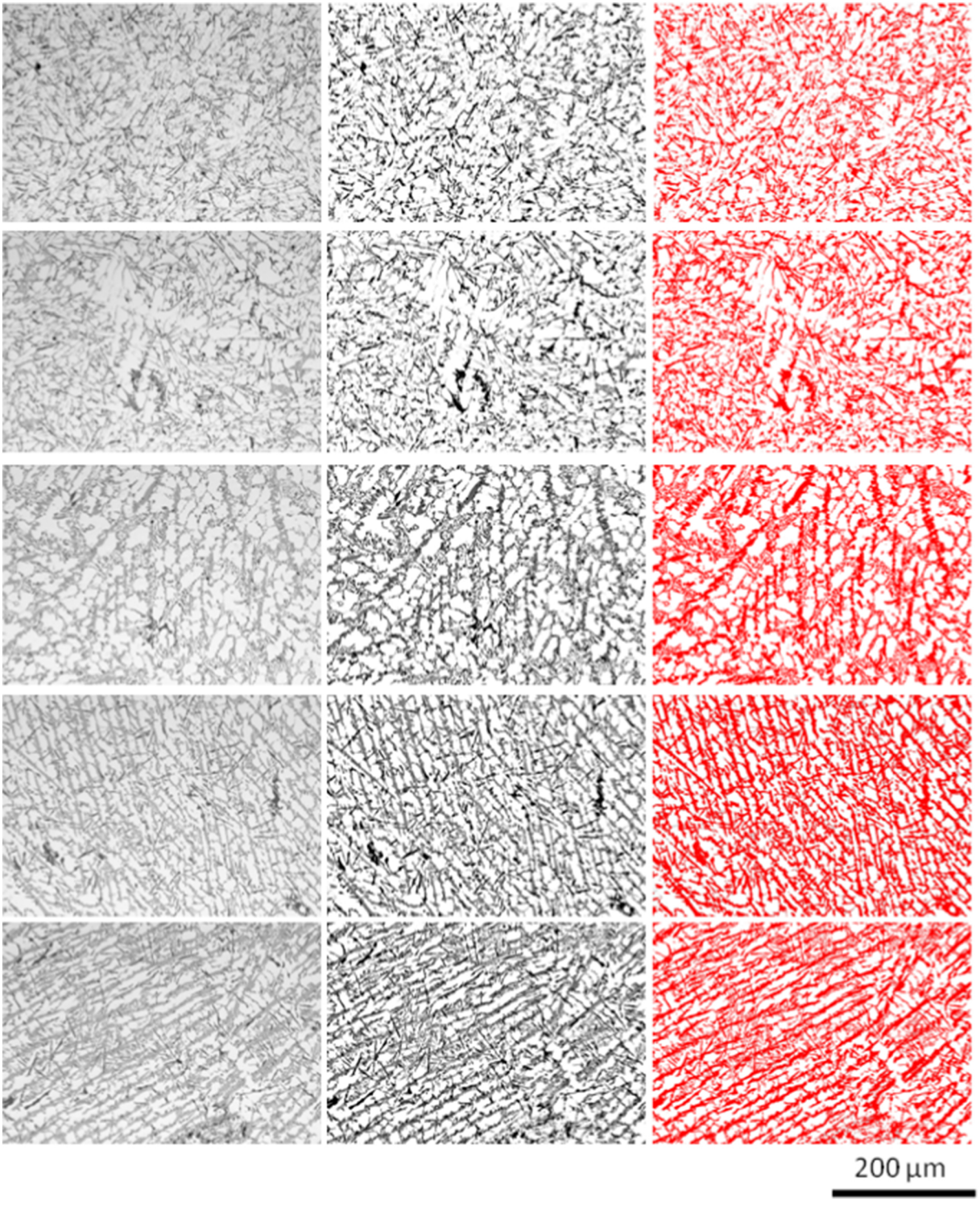

Figure 2

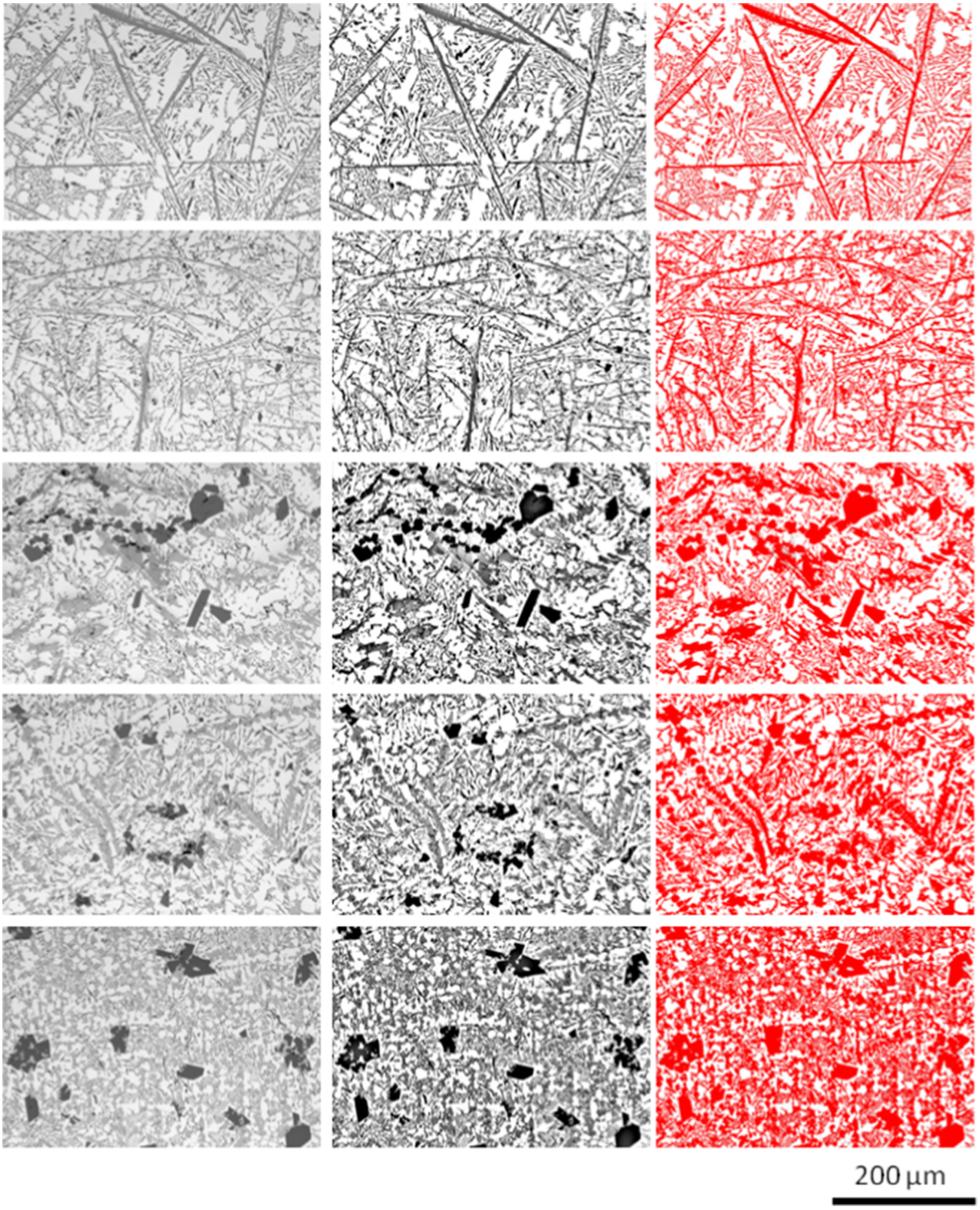

Figure 3

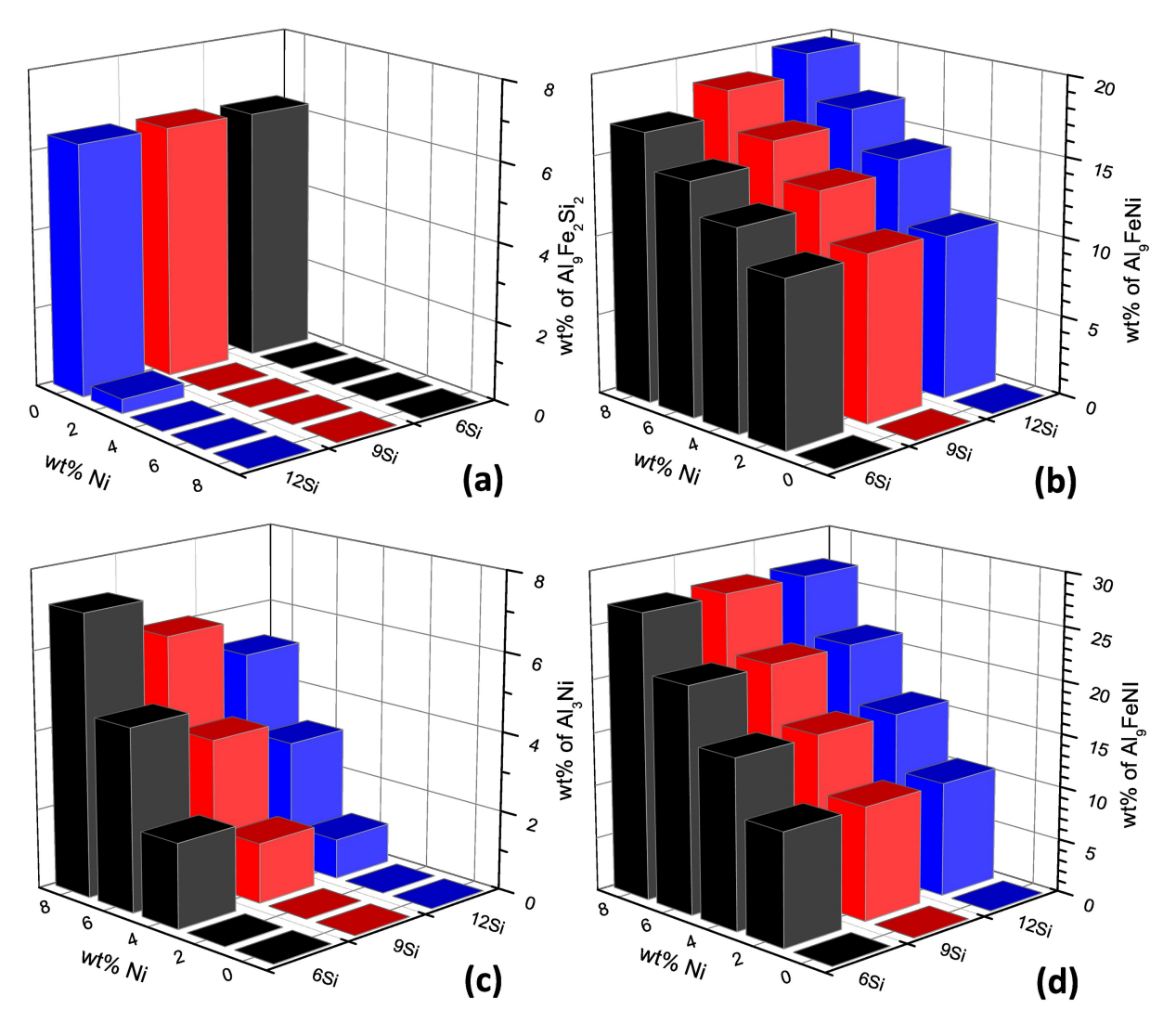
wt% Ni
0
2
4
6
8
6Si
9Si
12Si
wt% of $Al_9Fe_2Si_2$
0
2
4
6
8
(a)
wt% of Al_9FeNi
0
5
10
15
20
(b)
wt% of Al_3Ni
0
2
4
6
8
(c)
wt% of Al_9FeNI
0
5
10
15
20
25
30
(d)

Figure 4

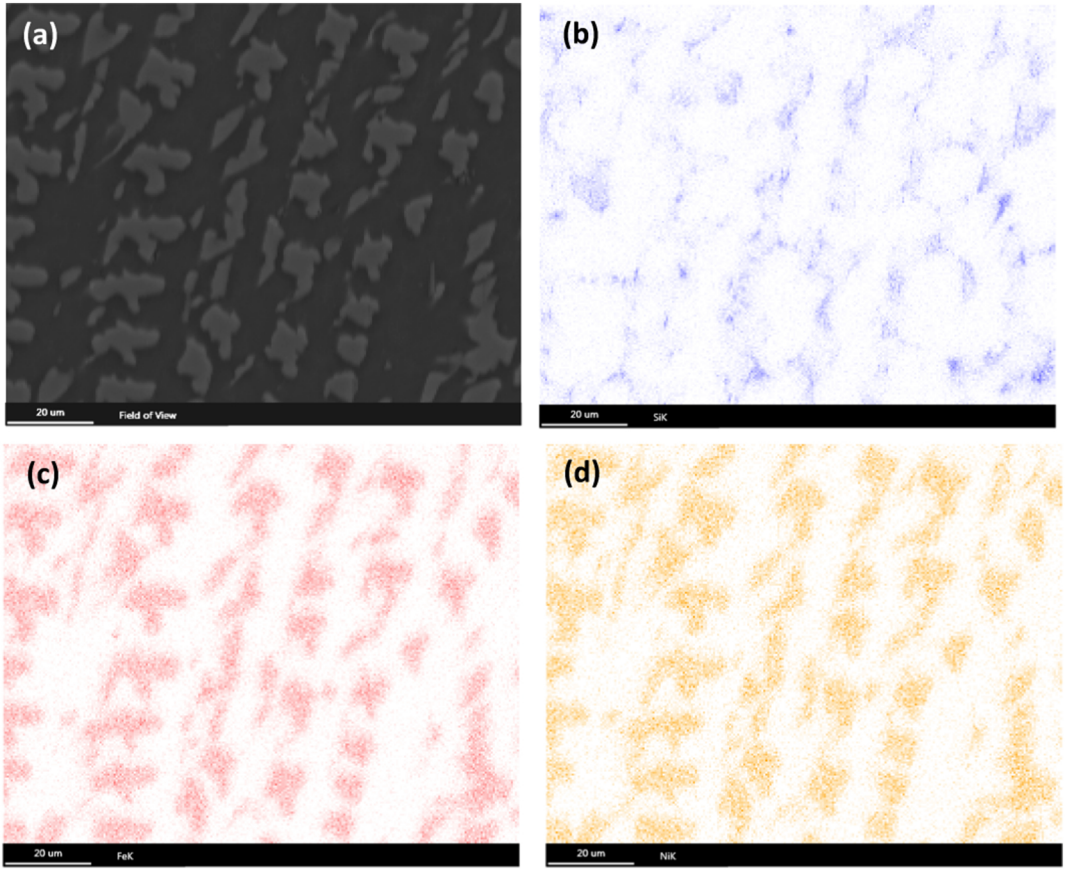

Figure 5

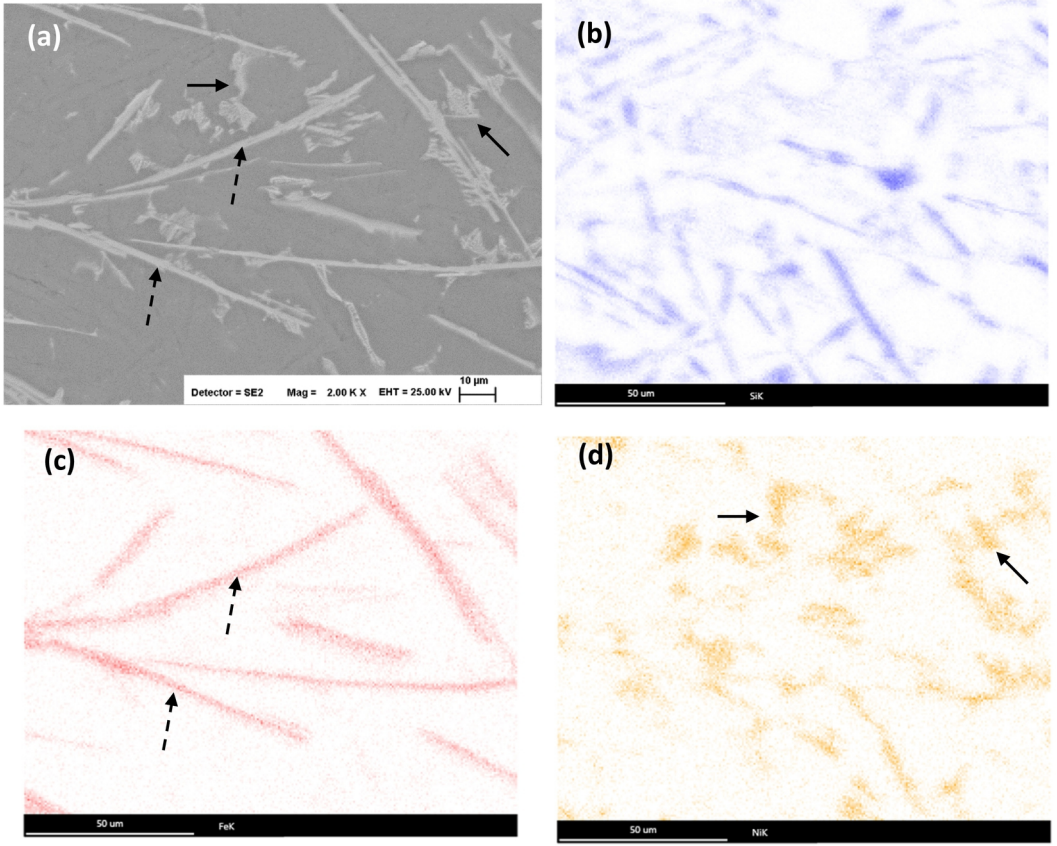
(a)
Detector = SE2
Mag = 2.00 K X
EHT = 25.00 kV
10 µm
(b)
50 um
SiK
(c)
50 um
FeK
(d)
50 um
NiK

Figure 6

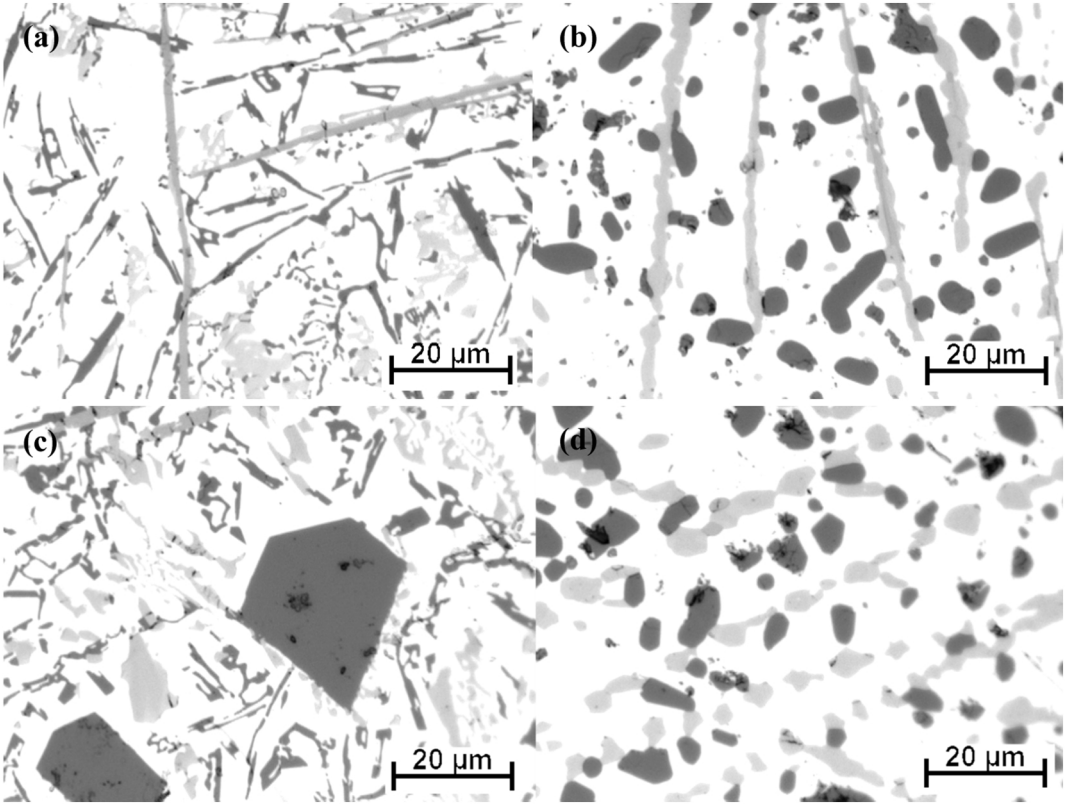

Figure 7

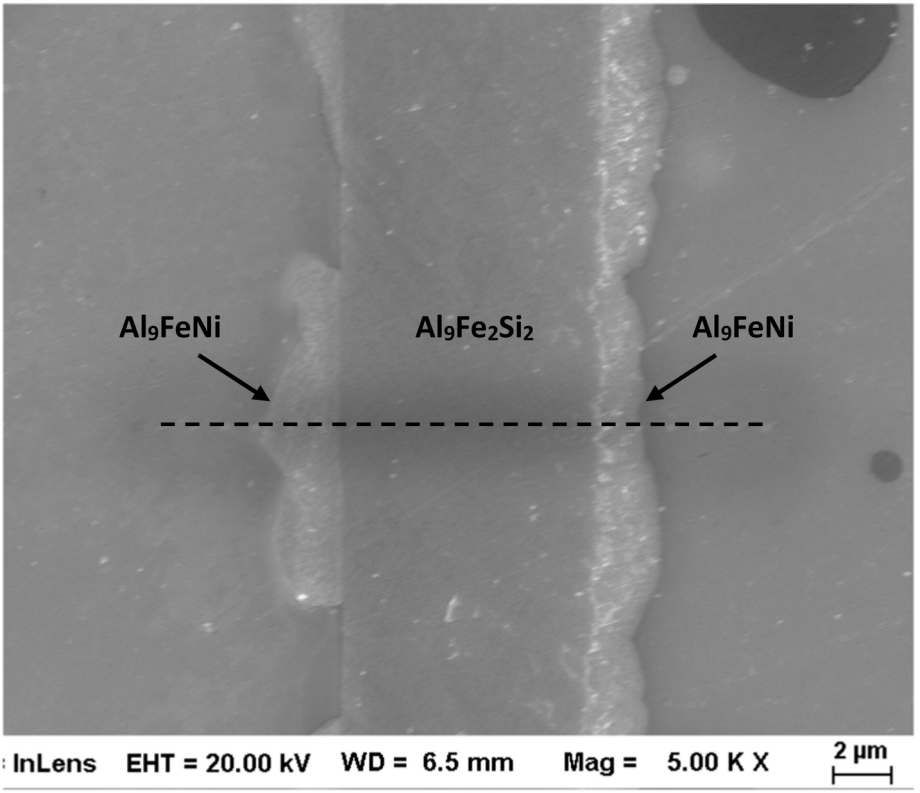
Al9FeNi
Al9Fe2Si2
Al9FeNi
InLens
EHT = 20.00 kV
WD = 6.5 mm
Mag = 5.00 K X
2 µm

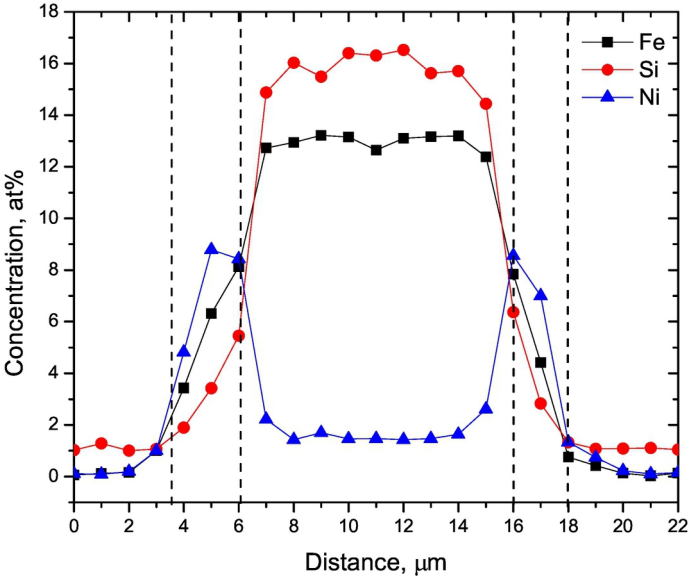
Fe
Si
Ni
Concentration, at%
Distance, µm
0
2
4
6
8
10
12
14
16
18
20
22

Figure 8

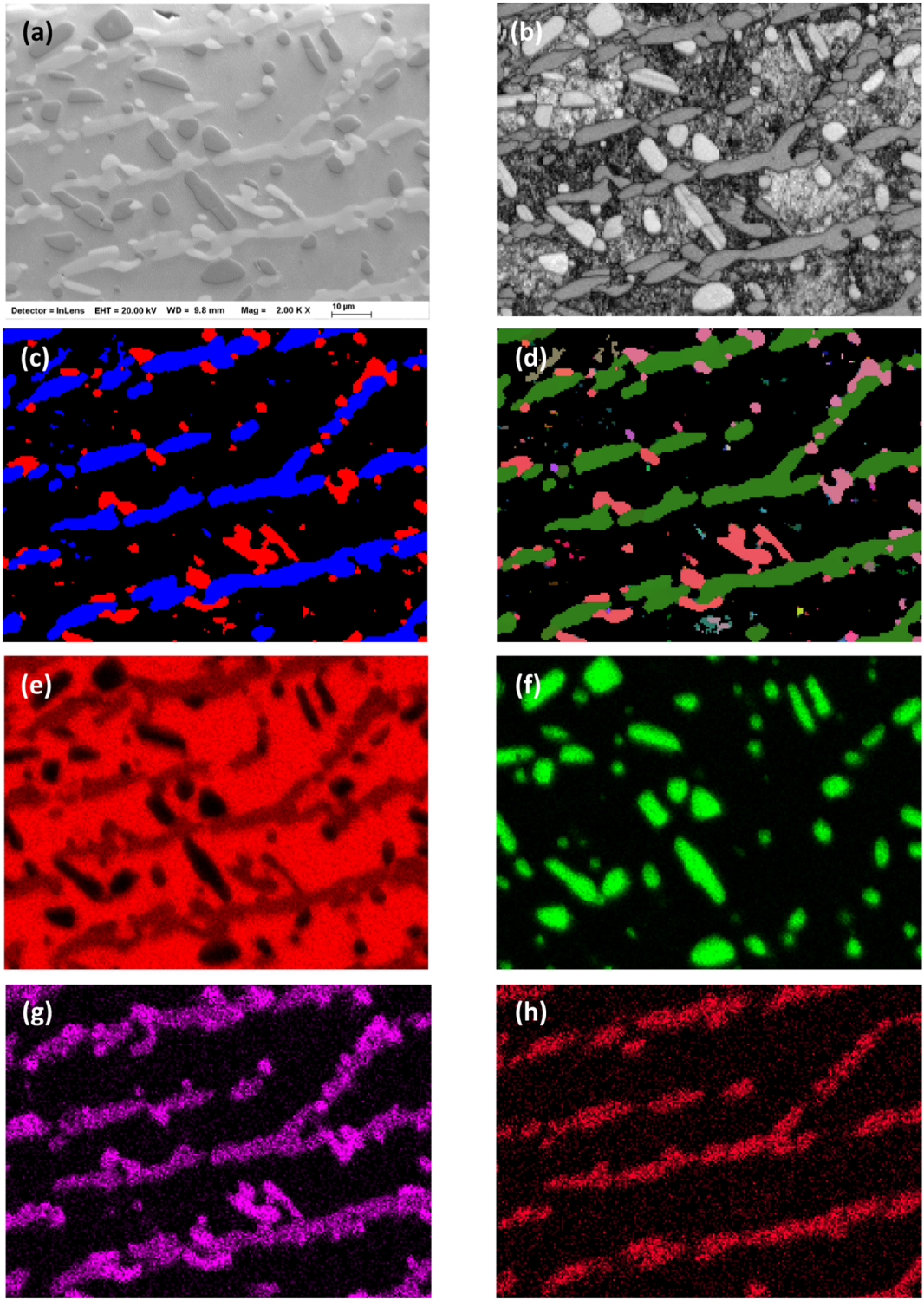

Figure 9

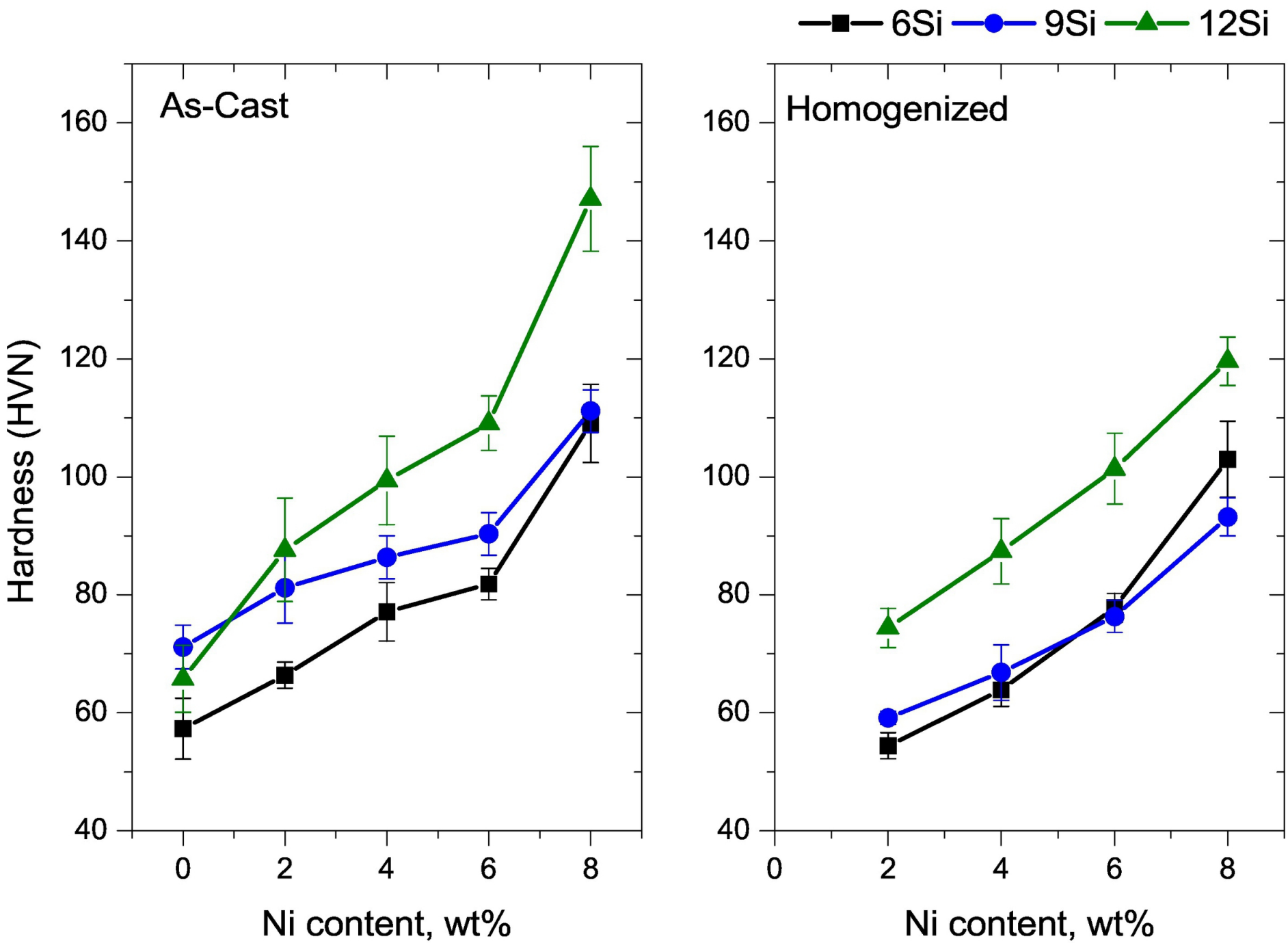
6Si
9Si
12Si
As-Cast
Homogenized
Hardness (HVN)
160
140
120
100
80
60
40
0
2
4
6
8
Ni content, wt%
Ni content, wt%

Figure 10

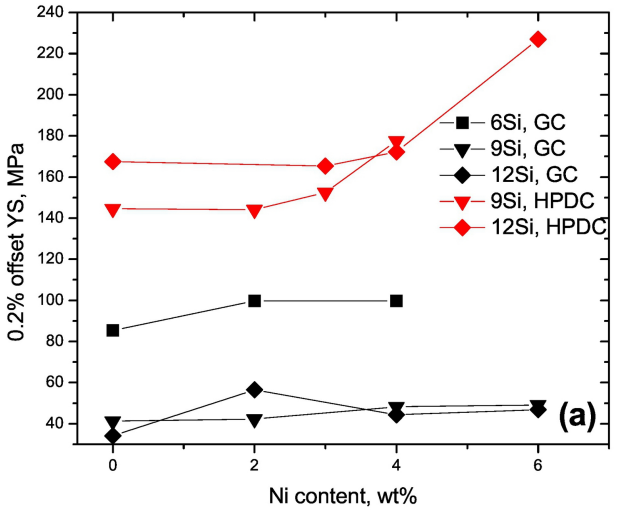
0.2% offset YS, MPa
Ni content, wt%
6Si, GC
9Si, GC
12Si, GC
9Si, HPDC
12Si, HPDC
(a)

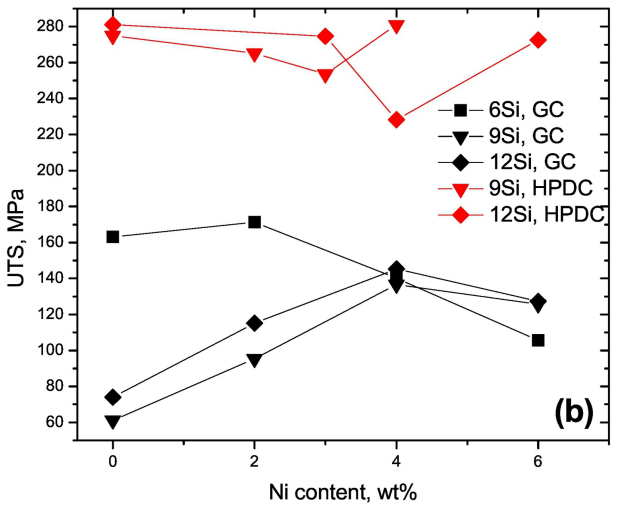
UTS, MPa
Ni content, wt%
6Si, GC
9Si, GC
12Si, GC
9Si, HPDC
12Si, HPDC
(b)

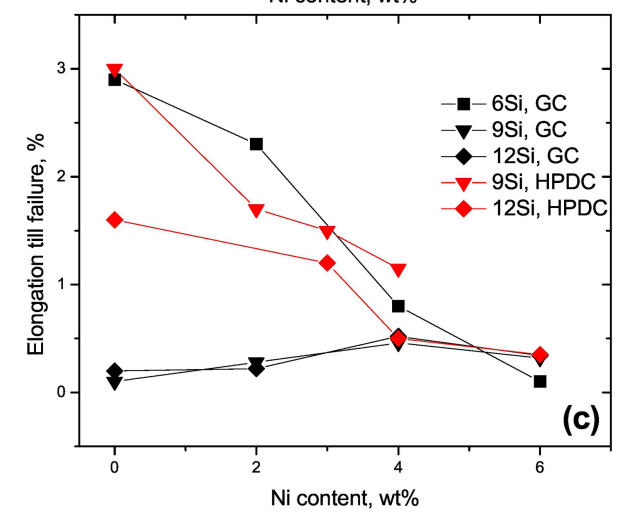
Elongation till failure, %
Ni content, wt%
6Si, GC
9Si, GC
12Si, GC
9Si, HPDC
12Si, HPDC
(c)

Figure 11